molecular pharmaceutics

pubs.acs.org/molecularpharmaceutics

Article

Spatially Defined Post-manufacturing Loading of Nanoparticles into Hydrogel-Forming Microneedles

Published as part of Molecular Pharmaceutics special issue "Recent Developments in Transdermal Microneedle Drug Delivery".

Alfonso Arguello, Gaurav Sadhnani, Jerry Leung, Fatma Moawad, Pieter R. Cullis, Sarah Hedtrich, and Davide Brambilla*

Cite This: *Mol. Pharmaceutics* 2025, 22, 4778–4793

Read Online

ACCESS | Metrics & More | Article Recommendations | Supporting Information

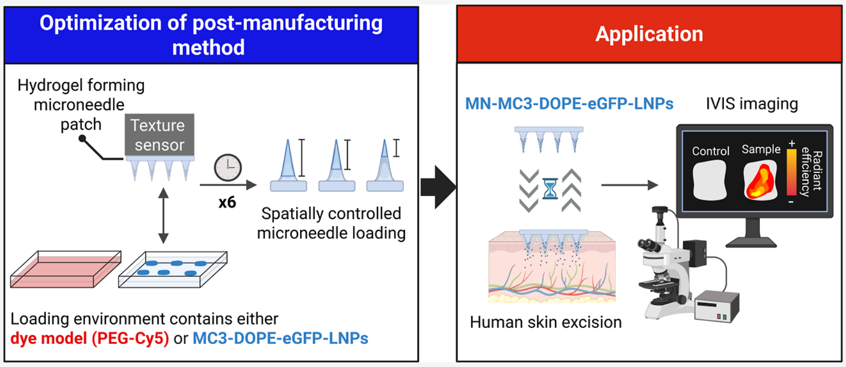

ABSTRACT: Efficient transdermal delivery of the genetic material remains a key challenge for noninvasive gene therapy due to skin's barrier properties. While lipid nanoparticles (LNPs) effectively encapsulate and protect mRNA, they cannot freely penetrate the skin. Hydrogel-forming microneedle (HFMN) patches, which swell upon skin insertion, offer a promising strategy to overcome this limitation. However, integrating fragile LNPs into HFMNs without compromising the patch integrity or nanoparticle function remains an unresolved issue. Here, we present a method for the spatially controlled, post-manufacturing loading of mRNA-encapsulated LNPs into HFMN patches. Key parameters—including the HFMN patch height (250, 500, and 800 μm), insertion depth, duration (15–60 s), and repetition (up to six times)—were systematically evaluated in an agarose gel containing a dye model to optimize loading while preserving the microneedle and overall patch integrity. Under optimized conditions, 500 μm HFMN patches loaded with either MC3-DOPE-DiI-LNPs or MC3-DOPE-eGFP-LNPs, at 400 μm insertion depth and 15 s hold time, achieved up to 140 μg of payload after six insertions. Ex vivo experiments using fluorescently labeled empty LNPs confirmed the nanoparticle release. Despite modest recovery, functional studies demonstrated the successful delivery and cellular uptake of functional LNPs into human skin, as confirmed by IVIS imaging. This approach offers a robust and minimally invasive method to load and deliver the genetic material through the skin, supporting the advancement of the microneedle-based transdermal gene therapy.

KEYWORDS: *mRNA-encapsulated lipid nanoparticles, hydrogel-forming microneedle patches, spatially controlled loading, texture analyzer, transdermal delivery, GFP transfection*

INTRODUCTION

The transdermal route is a minimally invasive drug delivery way that bypasses first-pass metabolism, reduces pain, and enhances patient compliance.[1−3] However, the stratum corneum (SC), the outermost skin layer, acts as a major barrier.[4] Composed mainly of corneocytes, it is 10−15 μm thick, preventing water loss and blocking external substances. Only drugs with low molecular weight (<500 Da) and moderate lipophilicity (log(P) 1−3) can passively diffuse through.[3,5−7] To overcome this barrier, microneedle (MN) patches have been developed. These microsized needles (100−2000 μm) puncture the SC without reaching dermal nerves or blood vessels, creating microchannels that enhance drug

Received: March 25, 2025
Revised: July 3, 2025
Accepted: July 3, 2025
Published: July 11, 2025

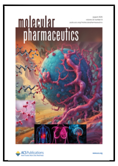

https://doi.org/10.1021/acs.molpharmaceut.5c00403

diffusion into the epidermis and dermis, improving systemic absorption.[4,8−11]

Various MN patches have been developed for drug delivery: solid, coated, dissolving, hollow, and hydrogel-forming microneedles (HFMNs).[4,12−14] Solid MNs create microchannels before drug application but often result in low efficiency and inconsistent dosing.[15] Coated MNs rely on a dissolvable surface layer; however, irregular coatings, low drug-loading capacity, and drug waste limit their performance.[16,17] Dissolving MNs embed drugs in a water-soluble matrix that dissolves upon skin insertion. Although biocompatible, limitations include poor delivery of hydrophobic or high-dose compounds and reduced mechanical strength when hygroscopic materials such as sugars are used.[18−20] Hollow MNs inject liquid drugs but can be obstructed when applied to thicker or less elastic skin.[21−23] Finally, HFMN patches, made from hydrophilic cross-linked polymers,[14,24] can deliver drugs by embedding them in the polymer matrix or loading them into a reservoir.[4,25] Common polymers include poly(methylvinylether-*co*-maleic acid) (PMVE/MA) and poly(methylvinylether-*co*-maleic anhydride) (PMVE/MAH), cross-linked with poly(ethylene glycol) (PEG).[26] Compared to other MN types, HFMNs are particularly well-suited for lipid nanoparticle (LNP) delivery due to their swelling behavior, biocompatibility, and tunable matrix. These properties allow gentle loading and controlled release of thermosensitive cargo such as mRNA (mRNA)-encapsulated LNPs, without requiring harsh fabrication steps that may compromise the nanoparticle stability.

In recent years, smart responsive hydrogels have also gained attention for enabling controlled drug release in response to stimuli such as temperature, pH, light, or electrical signals.[27−30] For instance, Wang et al. developed an injectable, conductive hydrogel for ischemic stroke treatment, demonstrating the potential of electrically assisted delivery.[31] Similar stimulus-responsive systems have already been explored in HFMNs for on-demand drug release.[27−30] Incorporating similar designs into MNs could enable the transdermal delivery of thermosensitive or complex biologics, such as LNP-mRNA. While our current system relies on passive loading and release, future work may integrate responsive mechanisms to improve precision and efficacy.

In parallel, the intra- and transdermal delivery of LNP-mRNA has been recognized for its ability to protect mRNA from nucleases and enhance cellular uptake. LNPs generally consist of ionizable lipids, cholesterol, phospholipids, and PEG-conjugated lipids.[32,33] Traditionally administrated via hypodermic injection, LNP-mRNA formulations have proven safe and effective in delivering the genetic material.[34] Once inside cells, the mRNA escapes the LNPs and initiates translation in the cytoplasm to produce therapeutic proteins.[34−36] Incorporating LNPs into MN patches could enhance the stability and enable localized RNA delivery for skin diseases. However, successful skin delivery depends on factors such as LNP stability, MN type, and loading method.[37]

Despite their therapeutic success, LNP-mRNA formulations face stability challenges due to temperature variations during transport and storage, requiring strict handling conditions to prevent degradation.[38] Therefore, manufacturing MN patches loaded with LNP-mRNA is complex, as both components are highly sensitive to environmental, chemical, and mechanical stresses. During premanufacturing, LNPs may interact with oppositely charged polymers, causing nanoparticle aggregation, while elevated temperatures (≥ 25 °C) required for solvent evaporation during patch solidification may further compromise stability.[39] Additionally, pH fluctuations during polymer solidification can alter the LNP membrane structure, as many components are sensitive to ionic changes, potentially reducing functionality.[39−42] Research on MN-based nucleic acid delivery, including mRNA, plasmid DNA, and small interfering RNA, remains limited. Exiting studies use solid, coated, dissolving, and hollow MNs with nucleic acids either naked or encapsulated in nonviral vectors (e.g., cationic polymer, liposome, protamine, PLGA-based nanoparticle, and LNPs).[37] To date, LNP-mRNA delivery has only been reported using dissolving MNs.[43] While post-manufacturing strategies such as dip-coating, spray-coating, or piezoelectric inkjet printing have been applied to solid MNs, they typically offer limited drug-loading capacity, uneven coating, and potential drug loss.[17] These limitations highlight the need for alternative post-manufacturing approaches that can accommodate higher payloads while preserving the structure and function of sensitive cargo.

To address this gap, we developed a method for spatially controlled loading of mRNA-encapsulated LNPs into prefabricated HFMN patches using a texture analyzer in compression mode. To optimize this approach, we employ MN patches of different heights, and quantification studies measured LNP loading, followed by ex vivo experiments to evaluate delivery into the skin. Subsequently, the MN loaded with MC3-DOPE-eGFP LNPs was applied to the human abdominal skin, confirming functional mRNA expression via IVIS imaging. To our knowledge, this is the first demonstration of LNP-mRNA delivery using HFMNs via a post-manufacturing method, offering a promising platform that overcomes the limitations of high-temperature exposure and enables efficient, stable, and targeted gene delivery to the skin.

■ MATERIALS AND METHODS

Materials. HFMN Patches Fabrication: Gantrez S97 (Ashland, Kidderminster, UK), sodium carbonate (Na_2CO_3, >99.7%, Fisher Chemical, Fair Lawn, NJ, US), polyethylene glycol 10 kDa (PEG 10 kDa, flakes form, Sigma-Aldrich, St. Louis, MO, US), poly(acrylic acid) 450 kDa (Sigma-Aldrich, St. Louis, MO, US), and distilled water. Preparation of agarose gels: Agarose powder, molecular biology grade, and low EEO/multipurpose (Fisher Bioreagents, Fair Lawn, NJ, US). Preparation of PEG-Cy5: Cy5-NHS (synthesized in our laboratory following a previously described protocol[44]), PEG-Amine (M-NH_2HCl-5000 MW 5000 g/mol, Jenkem Technology, Beijing, CN), triethylamine (99.0%, Anachemia Chemicals, Mississauga, ON, CA), dimethyl sulfoxide (DMSO, HPLC grade, 99.9%, Fisher Chemical, Fair Lawn, NJ, US), sodium chloride (NaCl, 99.0% Fisher Scientific, Fair Lawn, NJ, US), Milli-Q water (Milli-Q advantage A10, Millipore, Burlington, USA), and G-15 Sephadex (Cytiva BioProcess, Uppsala, SE). Preparation of lipid nanoparticles (LNPs): (6Z,9Z,28Z,31Z)-heptatriaconta-6,9,28,31-tetraen-19-yl-4-(dimethylamino)butanoate (DLin-MC3-DMA, Avanti Polar Lipids, Alabaster, AL, US), 1,2-dioleoylphosphatidylethanolamine (DOPE, Avanti Polar Lipids, Alabaster, AL, US), cholesterol (Sigma-Aldrich, St. Louis, MO, US), and 1,2-dimyristoyl-rac-*glycero*-3-methoxypolyethylene glycol-2000 (DMG-PEG 2000, Avanti Polar Lipids, Alabaster, AL, US). Buffer solutions: Phosphate-buffered saline (PBS, pH 7.4, Sigma-Aldrich, St. Louis, MO, US), sodium acetate (NaOAc, Sigma-Aldrich, St. Louis, MO, US), and anhydrous ethanol (Commercial Alcohols, Brampton, ON, CA). LNP Cargo: Enhanced green fluorescent protein mRNA (eGFP, CleanCap 5-methoxyuridine, TriLink Biotechnologies, San Diego, CA, US) and tetramethyl indocarbocyanine perchlorate (DiI, Invitrogen, Carlsbad, CA, US) were used for LNPs without nucleic acid cargo (empty). For ex vivo experiments: Excised porcine skin samples were kindly provided by the Faculty of Veterinary Medicine, University of Montreal, and stored at −20 °C until use. Excised human abdominal biopsies were obtained from healthy donors undergoing abdominoplasties at Helios-Klinikum Berl*in*-Buch, Germany, from the Clinic for Plastic and Aesthetic Surgery.

■ METHODS

Fabrication of the HFMN Patches. The manufacture of HFMN patches was carried out as previously described.[45] A polymeric mixture that comprises Gantrez S-97 (20% w/w), PEG 10 kDa (7.5% w/w), Na_2CO_3, (3% w/w), and poly(acrylic acid) 450 kDa (1.5% w/w) was prepared using 5 mL of ultrapure deionized water. The blend was centrifugated at 4500 rpm for 5 min at 21 °C; then, each 5 mL pf mixture was poured into 2 PDMS molds (Micropoint Technologies Pvt. Ltd., Singapore) for MN fabrication. For this experiment, we employed PDMS molds with 3 dimensions: a 10 × 10 pyramidal array with 250 μm needle height (H), 100 μm needle base width (B), and 250 μm needle pitch (P, or tip-to-tip spacing); a 10 × 10 pyramidal array with 500 μm H, 200 μm B, and 500 μm P; and a 10 × 10 pyramidal array with 800 μm H, 200 μm B, and 500 μm P. The molds were placed in 12-well plates, subsequently immersed in the polymeric mixture, and later centrifugated at 4000 rpm for 10 min at 21 °C. The centrifugation step was repeated 4 times, and then the molds were left to dry at room temperature for 24 h. In the meantime, the excess polymeric mixture in the 12-well plates was recovered and used to form a polymeric backing layer onto the 24 h-dried MNs in the molds. This backing layer will facilitate the complete detachment of the MN patches from the mold and further attachment to a cover glass for post-manufacturing loading with a dye or LNPs. To form the backing layer, the molds were placed into 12-well plates, dipped again in the polymeric mixture, and centrifuged at 4000 rpm for 5 min at 21 °C. The molds were left to dry at room temperature for 24 h and then placed in an oven for 48 h at 70 °C to facilitate the cross-linking reaction. This reaction involves an esterification reaction, forming an ester bond between the carboxylic acid groups from the copolymer Gantrez S-97 and poly(acrylic acid) 450 kDa and the hydroxyl groups from PEG 10 kDa. The MN patches were carefully demolded after the curing step was completed and kept at room temperature until used.

Preparation of the Agarose Gel Containing the Therapeutic Agent. The agarose gel plays a crucial role in the post-manufacturing loading approach. It acts as a supportive matrix to incorporate and retain a dye or nanoparticle that we want to load into the patches. The gel acts as a stable reservoir, allowing the controlled loading of the dye or nanoparticles when the MN patches come into contact with it. We prepared two types of agarose gels, the first mainly to optimize the loading method using a dye model, PEG-Cy5 (5 kDa), and another gel containing LNPs, whose preparation is described below.

Preparation of the Agarose Gel Containing PEG-Cy5 (5 kDa). For all experiments to optimize the post-fabrication loading approach, we prepared 1% (w/v) agarose gels by placing an appropriate amount of agarose powder and distilled water in an Erlenmeyer flask, sealing the flask using a stopper with a capillary tube, and then heating the mixture in a microwave. This setup enables efficient heat transfer and ensures that any pressure buildup within the flask can be released without disrupting the agarose solution. This method aids to maintain the integrity of the agarose gel preparation by providing a stable environment during the heating process with the microwave, while also reducing the loss of agarose mixture due to evaporation or spillage. The mixture was heated in the microwave in short intervals of 15 s until 1 min, swirling gently after each interval until the agarose completely dissolved and the solution appeared clear. Once dissolved, we allowed the agarose solution to cool to approximately 40−50 °C. We then added the appropriate amount of PEG-Cy5 (5 kDa) to the agarose solution, gently swirling the mixture by hand to ensure thorough mixing before carefully pouring it into a Petri dish (100 × 100 × 20 mm). The targeted concentrations of PEG-Cy5 (5 kDa) in the gels were 40, 80, 120, 160, and 200 μM. Afterward, we allowed the gel to cool to room temperature until it completely solidified. Once solid, the gels were ready for the post-manufacturing loading with the texture analyzer.

Preparation of the Agarose Gel Containing MC3-DOPE-DiI LNPs or MC3-DOPE-mGFP LNPs. The 1% w/v agarose gels were prepared following the same procedure as previously described, with the only difference being that the LNPs were not added to the clear agarose solution after microwaving. Instead, the agarose solution was poured directly into a Petri dish (100 × 100 × 20 mm) and allowed to cool to room temperature to solidify. Once the gel was fully solidified, 10 μL of either MC3-DOPE-DiI LNPs or MC3-DOPE-mGFP LNPs was carefully added to the surface of the gel and allowed to air-dry. Each 10 μL of LNPs added to the surface represented a single attempt to insert the MN patch into the agarose gel. After the LNPs were air-dried on the gels, the setup was ready for post-manufacturing MN patch loading using the texture analyzer.

Synthesis of PEG-Cy5. PEG-Cy5 was prepared following the previously described method.[44] Cy5-NHS (7.4 mg, 12 μmol, 2 equiv) and M-NH_2HCl (MW 5000, 30 mg, 6 μmol, 1 equiv) were dissolved in 1 mL of DMSO with a drop of triethylamine. The reaction mixture was stirred for 18 h, protected from light. Subsequently, the mixture was diluted with 20 mL of Milli-Q water and lyophilized. The residue was redissolved in 1 mL of 180 mM NaCl solution and purified using a G-15 Sephadex column. The combined fractions were lyophilized to yield PEG-Cy5 as a blue solid, which was diluted to the desired concentration for use.

Preparation of Lipid Nanoparticles. LNPs were prepared as previously described.[46] Briefly, the lipids DLin-MC3-DMA, DOPE, cholesterol, and DMG-PEG 2000, at 50/10/38.5/1.5 mol %, respectively, and 10 mM final lipid concentration, were dissolved in anhydrous ethanol and then rapidly mixed by T-junction with an aqueous solution at a 1:3 ratio (20 mL/min final flow rate). For LNPs containing mRNA encoding eGFP, the mRNA was first dissolved in a 25 mM NaOAc pH 4 buffer before rapid mixing with the ethanolic mixture of lipids (amine-to-phosphate ratio of 6), with the resulting solution dialyzed overnight against a 500-fold volume of 1× pH 7.4 PBS. For LNPs without any nucleic acid cargo (empty), 0.2 mol % of DiI was added to the initial lipid mixture before mixing with the 25 mM NaOAc pH 4 buffer and subsequently dialyzing overnight in a 500-fold volume 25 mM NaOAc pH 4 buffer. All LNPs were filter-sterilized with 0.2 μm Supor membrane syringe filters (Pall Corporation, Port Washington, NY) and concentrated in Amicon 10 kDa MWCO ultra centrifugal filters (EMD Millipore, Billerica, MA). The total lipid content was extrapolated using the Cholesterol E Kit (Wako Diagnostics, Richmond, VA), while encapsulation was determined using the Quant-it RiboGreen RNA Assay Kit (Thermo Fisher Scientific, Mississauga, ON, CA).

Procedure for Loading Manufactured HFMN Patches Using a Texture Analyzer. The texture analyzer was set up by selecting a probe with a flat, 6 mm diameter stainless-steel cylinder for the post-manufacturing loading of the HFMN patches. The instrument was calibrated by adjusting both the force and the height, with the probe positioned 40 mm from the stainless-steel base of the analyzer. The experimental library "hold until time" was chosen for all loading experiments, with consistent testing conditions: a pretest speed of 1 mm/s, a test speed of 2 mm/s, a post-test speed of 10 mm/s, and a trigger force of 0.049 N. The procedures for securing the blank HFMN patch to the probe involved attaching it to a cover glass using a double-sided tape. After the patch was firmly fixed to the cover glass, the entire assembly was attached to the probe of the texture analyzer, again utilizing a double-sided tape. The MN tips were oriented toward the stainless-steel base of the texture analyzer. Following this, the texture analyzer was set to move the probe downward toward the base, where an agarose gel (1% w/v) containing either a dye model, PEG-Cy5 5 kDa, or LNPs (MC3-DOPE-DiI LNPs or MC3-DOPE-mGFP LNPs) had been placed. The MN patch is inserted into the agarose gel at a specified depth and held in position for a specified time, after which the probe returns to its initial position. The MN patches loaded with PEG-Cy5 5 kDa or MC3-DOPE-DiI LNPs were stored at 4 °C until further characterization. Meanwhile, the MN patches loaded with MC3-DOPE-mGFP LNPs were kept at −80 °C until further analysis.

Optimization of the Post-manufacturing Loading Approach for HFMN Patches Using a Texture Analyzer. To optimize the post-manufacturing loading approach, we utilized PEG-Cy5 (5 kDa) as a model dye for loading into the HFMN patches. This process involved fine-tuning several critical parameters, such as adjusting the insertion depth into agarose gels containing PEG-Cy5, optimizing the duration for which the MNs remained within these gels, varying the concentration of PEG-Cy5 in the agarose gels, and performing multiple insertions to further enhance the loading capacity. These optimizations were intended to maximize the amount of PEG-Cy5 loaded into the MN patches while ensuring that they maintain their structural integrity, which is essential for efficient skin penetration.

Studying the Effect of Penetration Depth and Holding Time in the Agarose Gels Containing PEG-Cy5 (5 kDa) When Loading HFMN Patches. Agarose gels (1% w/v) containing the model dye PEG-Cy5 (5 kDa) at a concentration of 40 μM were prepared. Moreover, MN patches with three different needle heights (250, 500, and 800 μm) were manufactured. All of the patches were attached to the probe of the texture analyzer as previously described. As shown in Table 1, the texture analyzer was configured to insert the MN tips into the gel at specific depths based on each MN patch dimension: 50, 100, and 200 μm for MNs with a height of 250 μm; 100, 200, 300, and 400 μm for MNs with a height of 500 μm; and 200, 400, and 600 μm for MNs with a height of 800 μm. Each MN patch was inserted into the gel at the designated depth and held in position for 15, 30, 45, or 60 s.

Table 1. Experimental Conditions to Evaluate the Effect of the Insertion Depth and Holding Time in the Agarose Gels Containing PEG-Cy5 (5 kDa) with a Concentration of 40 μM on the Loading of HFMN Patches

sample	needle height [μm]	insertion depth [μm]	holding time [s]
A1	250	50	15
B1			30
C1			45
D1			60
E1		100	15
F1			30
G1			45
H1			60
I1		200	15
J1			30
K1			45
L1			60
A2	500	100	15
B2			30
C2			45
D2			60
E2		200	15
F2			30
G2			45
H2			60
I2		300	15
J2			30
K2			45
L2			60
M2		400	15
N2			30
O2			45
P2			60
A3	800	200	15
B3			30
C3			45
D3			60
E3		400	15
F3			30
G3			45
H3			60
I3		600	15
J3			30
K3			45
L3			60

Studying the Effect of Tuning the Concentration of PEG-Cy5 (5 kDa) in the Agarose Gels on the Loading of HFMN Patches. Agarose gels (1% w/v) containing PEG-Cy5 (5 kDa) at concentrations of 40, 80, 120, 160, and 200 μM were prepared. Moreover, MN patches with a needle height of 500 μm were manufactured and selected based on the results of the previous experiment, which indicated that this height provides optimal balance between dye uptake efficiency and structural integrity of the MN patches. All the patches were attached to the probe of the texture analyzer as previously described. The texture analyzer was set to insert the MN tips into the gel at a depth of 400 μm and to maintain this position for 15 s, as shown in Table 2.

Table 2. Experimental Conditions to Evaluate the Effect of the Concentration of PEG-Cy5 (5 kDa) in Agarose Gels when Loading HFMN Patches

sample	needle height [μm]	insertion depth [μm]	holding time [s]	concentration of PEG-Cy5 in agarose gel 1% (w/v) [μM]
A	500	400	15	40
B				80
C				120
D				160
E				200

Studying the Effect of Performing Multiple Insertions in Agarose Gels Containing PEG-Cy5 (5 kDa) on the Loading of HFMN Patches. Agarose gels (1% w/v) containing PEG-Cy5 (5 kDa) at 40 μM were prepared. Additionally, MN patches with a needle height of 500 μm were also prepared. As previously mentioned, all patches were attached to the texture analyzer probe. The texture analyzer was set so that the MN tips were inserted into the gel at a depth of 400 μm and held in this position for either 15 or 60 s, as shown in Table 3. At the end of the specified holding time, the MN patches were allowed to air-dry for 5 min before the procedure was repeated. This allowed multiple applications or insertions into the agarose gels to assess how the loading capacity and structural integrity of the patches were affected.

Table 3. Experimental Conditions to Evaluate the Effect of Multiple Insertions in Agarose Gels Containing PEG-Cy5 (5 kDa) on the Loading of HFMN Patches

sample	needle height [μm]	insertion depth [μm]	holding time [s]	concentration of PEG-Cy5 in agarose gel 1% (w/v) [μM]	times inserted in the agarose gel
A	500	400	15	40	1
B					3
C					6
D			60		1
E					3
F					6

LNPs Loading into HFMN Patches by the Post-manufacturing Approach. The post-manufacturing loading of LNPs into HFMN patches followed a similar approach to the dye-loading method. Two types of LNPs, MC3-DOPE-DiI and MC3-DOPE-mGFP, were loaded. For each type, a 10 μL volume was applied to a solid 1% (w/v) agarose gel and air-dried on its surface before the MN patch was inserted. All patches were fixed to the texture analyzer probe, as previously described. Table 4 shows the texture analyzer settings, where MN tips were inserted to a depth of 400 μm and held in position for 15 s. Each patch was subjected to up to six insertions into the 1% agarose gel with a 5 min interval maintained between consecutive insertions.

Table 4. Experimental Conditions for Post-manufacturing Loading HFMN Patches through Multiple Insertions into Agarose Gels Containing LNPs

sample	needle height [μm]	insertion depth [μm]	holding time [s]	times inserted in the agarose gel
A	500	400	15	1
B				2
C				3
D				4
E				5
F				6

Characterization of Loaded Microneedles Using a Stereomicroscope. In all experiments, the HFMN patches were characterized by using a stereomicroscope (ApoTome.2, ZEISS) equipped with a back-illuminated sCMOS camera (Prime 95B, Photometric, ZEISS). Brightfield images were captured to assess the height and integrity of the MNs at zero and 90° before and after loading. Moreover, we used two types of high-efficiency filters, each filter mounted in a reflector module to measure the height of the needles and the whole integrity of the patch loaded with either the dye model, PEG-Cy5 (5 kDa), or MC3-DOPE-DiI LNPs. A filter with an excitation bandpass of 640/30 nm, a beamsplitter filter of 660 nm, and an emission bandpass of 690/50 nm (Filter Set 50; 488050-9901, Carl ZEISS Microscopy) was used to capture the images of the PEG-Cy5-loaded MN patches. Cy5 is a far-red fluorescent dye with an excitation wavelength band with a maximum peak at 646 nm and an emission band with a maximum peak at 664 nm. Meanwhile, another filter (Filter Set 63; 489063-0000, Carl ZEISS Microscopy) with an excitation bandpass of 572/25 nm, a beamsplitter filter of 590, and an emission bandpass of 629/62 nm was used to image the MC3-DOPE-DiI LNPs-loaded MN patches. DiI is a lipophilic membrane dye with an excitation band with a maximum peak at 551 nm and an emission band with a maximum peak at 565 nm.

Particle Size and Surface Charge Characterization. The hydrodynamic diameter, polydispersity index (PDI), and zeta potential of MC3-DOPE-DiI LNPs and MC3-DOPE-DiI LNP-loaded HFMNs were measured using a Zetasizer Nano ZS (Malvern Instruments, UK) equipped with a 633 nm laser and a detection angle of 173°. For size measurements, MC3-DOPE-DiI LNPs were diluted 1:10 in distilled water and loaded into a disposable 40 μL UV microcuvette (Cat. No. 03840300, BRAND). To assess the LNP release from HFMNs, patches were immersed in 1 mL of distilled water, and the resulting supernatant was recovered and used for analysis. Zeta potential measurements were carried out using folded capillary zeta cells (DTS1070, Malvern Instruments). All measurements were conducted at 25 °C, using the viscosity and refractive index of water as analysis parameters (material absorption: 0.010; material refractive index: 1.49). For each sample, five independent measurements were performed, each consisting of at least 10 runs. Results are reported as the mean ± standard deviation (SD).

Quantification of the Dye or LNPs Loaded in the HFMN Patches. *Quantification of PEG-Cy5 (5 kDa) Loaded into the HFMN Patches.* The amount of PEG-Cy5 (5k Da) in all HFMN patches, loaded under different conditions, shown in Tables 1−3, was quantified. In detail, each patch was placed in 1 mL of DMSO in a 2 mL microcentrifuge tube and incubated at 70 °C overnight to dissolve. The following day, the tubes were removed from the oven and allowed to cool to room temperature, and the solutions showed a reddish tint. Fluorescence intensity was then measured using a Spark

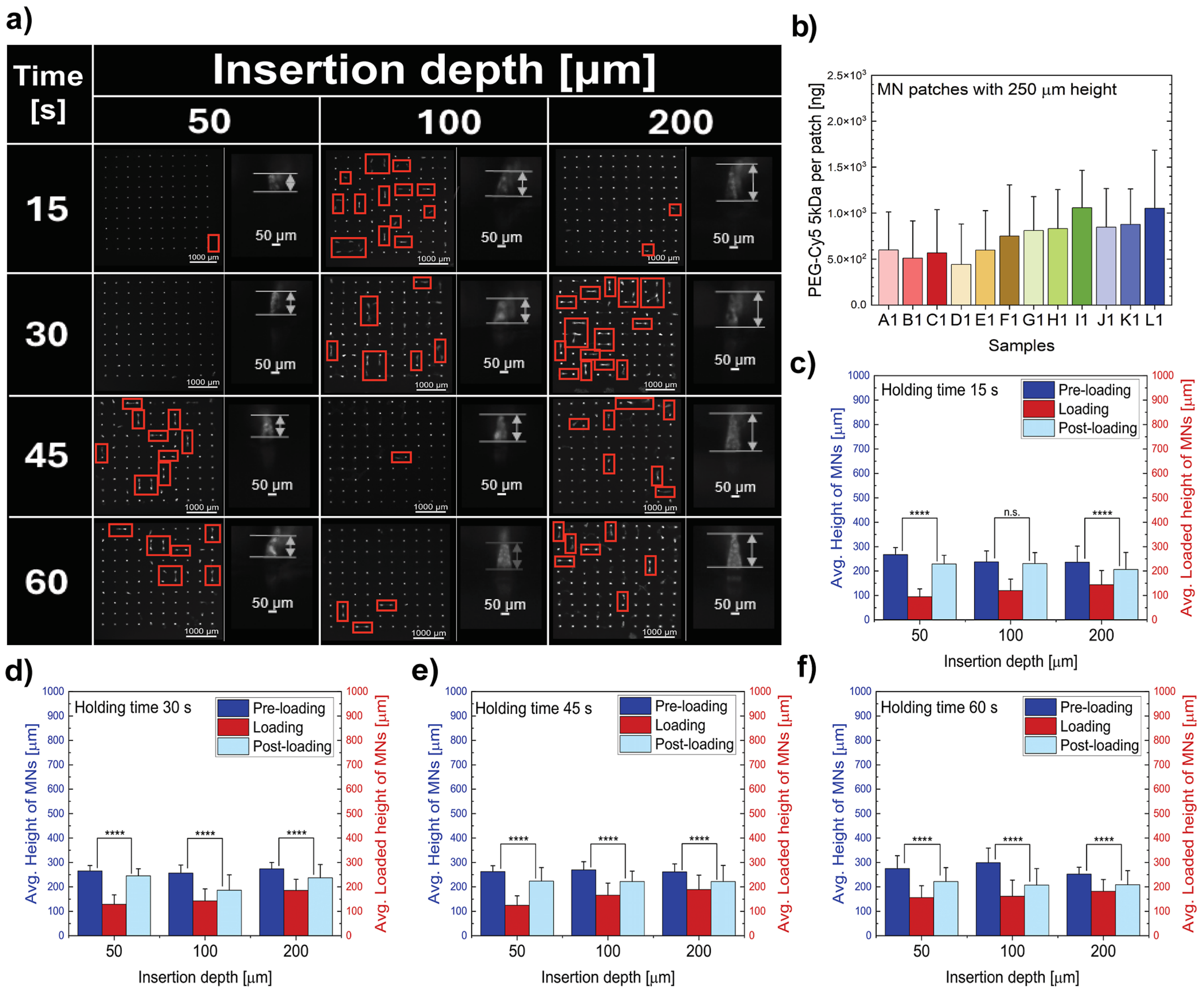

Figure 1. (a) Images of HFMN patches, with a needle height of 250 μm, inserted into 1% w/v agarose gels containing 40 μM PEG-Cy5 (5 kDa) at varying depths of 50, 100, and 200 μm. The patches were held at each depth for 15, 30, 45, and 60 s. Images were captured at zero degrees, with insets showing 90-degree zoomed-in views to highlight loaded needle tips under the respective conditions. Structural defects, such as needle twisting or fusion, are indicated within the red boxes. (b) Quantification of PEG-Cy5 (5 kDa) dye loaded in MN patches under the different insertion depths and hold times. The conditions included 50 μm insertion depth for 15 s (A1), 30 s (B1), 45 s (C1), and 60 s (D1); 100 μm insertion depth for 15 s (E1), 30 s (F1), 45 s (G1), and 60 s (H1); and 200 μm insertion depth for 15 s (I1), 30 s (J1), 45 s (K1), and 60 s (L1). Comparison of MN height before loading (dark blue) and after loading (light blue), with the average loaded height (red) achieved at varying insertion depths and holding times: 15 s (c), 30 s (d), 45 s (e), and 60 s (f). Error bars, mean ± SD (n = 3).

multimode fluorescence microplate reader (Tecan Group, Ltd., Männedorf, Switzerland). The measurement conditions included an excitation wavelength of 630 nm, an emission wavelength of 675 nm, a gain of 80, and a Z-position of 20000 μm using a black 96-well plate with an untreated, nonsterile surface. The obtained fluorescence intensity was used to calculate PEG-Cy5 (5 kDa) concentrations using a calibration curve, which was prepared by adding a known volume of 1 mM PEG-Cy5 (5 kDa) directly to the patches, allowing them to dry, and then dissolving the samples as previously described to ensure the consistency of quantification.

Quantification of the MC3-DOPE-DiI LNPs Loaded into the HFMN Patches. The HFMN patches loaded with the MC3-DOPE-DiI LNPs, as shown in Table 4, were immersed in methanol and left for 2 h under agitation to extract the DiI from the LNP membrane. The fluorescence intensity of DiI was then measured using a multimode fluorescence microplate reader. Measurement conditions included an excitation wavelength of 530 nm, an emission wavelength of 580 nm, a gain of 100, and a Z-position of 20000 μm, using a black 96-well plate with an untreated, nonsterile surface. A calibration curve was prepared by adding a known volume of 10 mM MC3-DOPE-DiI LNPs directly to the patches, drying, and extracting DiI from the LNP membrane as previously described to ensure consistent quantification.

LNP Delivery to Ex Vivo Skin Samples. *Preparation and Characterization of Skin Samples for Ex Vivo Experiments with HFMN Patches Loaded with MC3-DOPE-DiI LNPs.* To study the release of LNPs, initially, porcine abdominal skin samples were used. The skin was shaved to remove any hair that could interfere with MN patch application. The skin samples were then trimmed to remove excess adipose and connective tissue and sectioned into 1 cm × 1 cm pieces for experimental use. The skin was then acclimated at 32 °C for 1 h prior to starting the experiment. A spring applicator (Micropoint Technologies Pvt. Ltd., Singapore) was used to apply the MN patch to the skin, with the needles oriented toward the skin and the patch secured to the applicator with an adhesive tape. After patch application, the samples were left in contact with MC3-DOPE-DiI LNP-loaded patches for 1, 6, and 24 h. After each time interval, the patches were removed and characterized using a stereomicroscope, with images captured at a zero-degree angle in both the brightfield mode and fluorescence mode using the 63 filter Set.

Quantification of the Delivered Amount of MC3-DOPE-DiI LNPs into the Skin Samples. To quantify the amount of LNPs released into the porcine skin samples, DiI from the LNP membrane was extracted. The treated skin samples with the MC3-DOPE-DiI LNP-loaded HFMN patches were placed in 15 mL Falcon tubes with 1 mL of methanol and agitated overnight. The next day, fluorescence intensity was measured in a black 96-well plate with an untreated, nonsterile surface using a multimode fluorescence microplate reader set to excitation at 530 nm, emission at 580 nm, gain at 100, and Z-position at 20000 μm. A calibration curve was generated by adding a known volume of 10 mM MC3-DOPE-DiI LNPs directly to the skin samples, drying, and extracting DiI from the MC3-DOPE-DiI LNPs in the skin samples, as previously described, to ensure consistent quantification.

IVIS Imaging and Quantification of Functional mRNA Expression in Human Skin. *In Situ MN-Assisted LNP Delivery in Excised Human Skin.* Freshly excised human abdominal biopsies were obtained from healthy donors undergoing abdominoplasties at the Helios-Klinikum Berlin-Buch, Germany, from the Clinic for Plastic and Aesthetic Surgery (written consent obtained; ethics approval EA1/356/21). Excess adipose and connective tissue were previously removed. Skin pieces were cultured in transwells (Corning Life Sciences, Cat. No. 353093) inserted into a 6-well plate (Corning Life Sciences, Cat. No. 353502) with 1% penicillin and streptomycin-supplemented medium (Thermo Fisher Scientific, cat. no. MEPI500CA) in the outer wells. The skin surface was gently wiped with saline and 70% ethanol, and HFMNs loaded with LNP-GFP mRNA were inserted. After 24 h, the MN patches were removed, and skin biopsies were prepared for imaging.

To measure functional mRNA expression following insertion of LNP-GFP-mRNA-loaded HFMNs in human skin, an IVIS system (PerkinElmer, USA) was used. Skin biopsies were positioned on a black, low-fluorescence XFM-1 imaging mat (PerkinElmer, USA) for analysis using an IVIS Lumina imaging system (PerkinElmer, USA). Imaging settings were adjusted to optimize fluorescence signal detection with either medium or large binning and an f-stop of 1/8. Excitation and emission filters were 465/520 for GFP. The exposure time was 1 s. Uniform imaging parameters, including the field of view, filter configurations, and exposure times, were applied to all samples to ensure consistency for comparative purposes. Background signals and autofluorescence were minimized using the system's software tools. During post-imaging analysis, regions of interest (ROIs) were manually delineated for each human skin sample, and fluorescence intensity within each ROI was calculated as total radiant efficiency ($[p/s]/[\mu W/cm^2]$). Fluorescence intensity data from the treatment group were normalized to the average values of the control groups and expressed as fold changes. These fold-change measurements were assessed for statistical significance using 0.05, with a total of three independent biological replicates.

Statistical Analysis. Statistical analyses were conducted using GraphPad Prism (version 8.4.0; GraphPad Software, San Diego, CA) for data processing and interpretation throughout the study. Depending on the experimental design, either a one-way analysis of variance followed by Tukey's multiple comparisons test or a *t*-test was used. Results were considered statistically significant at a p-value <0.05. All experiments were performed in triplicate ($n = 3$), and data are presented as mean ± SD. Statistical significance was denoted as follows: (*) $p < 0.05$, (**) $p < 0.01$, (***) $p < 0.001$, and (****) $p < 0.0001$, while nonsignificant differences were marked as n.s.

■ RESULTS

MN patches with nominal needle heights of 250, 500, and 800 μm were used to optimize the post-manufacturing loading method. After fabrication, 10 × 10 arrays of pyramidal MNs were obtained with heights of 263 ± 17, 440 ± 11, and 679 ± 22 μm, reflecting slight alterations due to water evaporation during curing at 70 °C.[37] MN patches were inserted into a 1% w/v agarose gel containing PEG-Cy5 with a concentration of 40 μM at specified insertion depths and held for defined durations, as shown in Table 1. Fluorescence images captured at a zero-degree angle and 90-degree angles reveal the impact of insertion depth and holding time on dye uptake, highlighting how these factors influence loading efficiency and needle integrity.

As shown in Figure 1a, deeper insertion of HFMN patches into agarose gels and longer holding times resulted in an increased fluorescence intensity. Zero-degree angle images show brighter needles with deeper insertion and longer holding times. Similarly, 90-degree angle images demonstrate a clear correlation between insertion depth and holding time with enhanced dye loading, where needles appear brighter with longer dye-loaded regions in the needles. These observations align with the PEG-Cy5 concentrations obtained from dissolving PEG-Cy5-loaded MN patches with a 250 μm needle height, as shown in Figure 1b. When HFMN patches were held in agarose gels for 15 s, no clear trend in dye uptake was observed, with dye loading ranging from 500 to 600 ng for insertion depths of 50, 100, and 200 μm. However, as the holding time increased to 30, 45, and 60 s, dye uptake increased alongside insertion depth.

Figures 1c−f depicts the average needle height before and after insertion of 250 μm HFMN patches into the agarose gel at depths of 50, 100, and 200 μm for 15, 30, 45, and 60 s. Across all conditions, the needle height decreased by 19.8 ± 11.9% compared to the initial value. Notably, longer insertion times of 45 and 60 s led to a greater reduction of 25.9 ± 12.3%, while shorter insertions times of 15 and 30 s resulted in a smaller reduction of 13.6 ± 8.3%. The analysis of average loaded needle height with PEG-Cy5 (Figure 1c−f) shows that both insertion depth and holding time significantly affect HFMN loading. As the insertion depth increases from 50 to 200 μm, the average loaded height consistently rises, with the longest holding time amplifying this effect to between approximately 130 and 180 μm. For example, at 15 s (Figure 1c), the loaded height ranged from 83 ± 27 μm to 134 ± 52 μm, while at 60 s (Figure 1f), it increased to 145 ± 45 μm to 174 ± 44 μm.

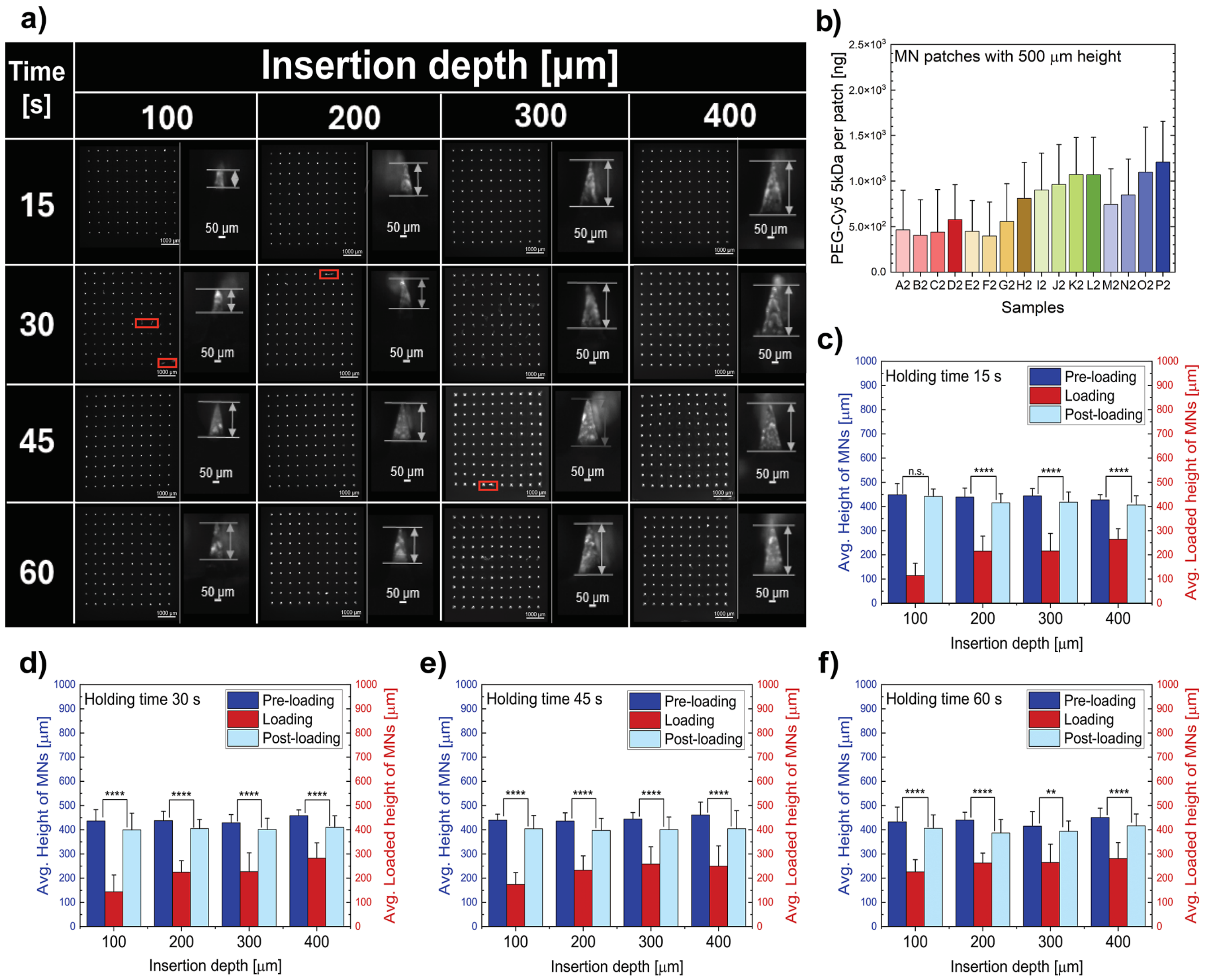

Figure 2. (a) Images of HFMN patches with a needle height of 500 μm inserted into 1% w/v agarose gels containing 40 μM PEG-Cy5 (5 kDa) at varying depths from 100, 200, 300, and 400 μm and held at each depth for 15, 30, 45, and 60 s. Images captured at zero degrees, with insets showing 90-degree zoomed views to highlight loaded needle tips under respective conditions. Structural defects, such as needle twisting or fusion, are indicated within the red boxes. (b) Quantification of PEG-Cy5 (5 kDa) dye loaded in MN patches under different insertion depths and hold times. The conditions included 100 μm insertion depth for 15 s (A2), 30 s (B2), 45 s (C2), and 60 s (D2); 200 μm insertion depth for 15 s (E2), 30 s (F2), 45 s (G2), and 60 s (H2); 300 μm insertion depth for 15 s (I2), 30 s (J2), 45 s (K2), and 60 s (L2); and 400 μm insertion depth for 15 s (M2), 30 s (N2), 45 s (O2), and 60 s (P2). Comparison of MN height before loading (dark blue) and after loading (light blue), with the average loaded height (red) achieved at varying insertion depths and holding times: 15 s (c), 30 s (d), 45 s (e), and 60 s (f). Error bars, mean ± SD ($n = 3$).

HFMN patches with a needle height of 500 μm were also evaluated to further explore the relationship between insertion depth, holding time, and structural integrity in the post-manufacturing loading process. The patches were tested at insertion depths of 100, 200, 300, and 400 μm with holding times of 15, 30, 45, and 60 s. Figure 2a displays the images of the HFMN arrays captured at a zero angle and side views at 90°, revealing increased brightness with longer holding times and deeper insertions, along with minimal torsion or fusion defects. Quantitative analysis of dye uptake, shown in Figure 2b, confirms that deeper insertions result in higher dye uptake across all holding times. These findings suggest that greater insertion depths enhance the interaction between the needles and agarose gel, improving dye absorption. The increased surface area exposed at deeper insertion depths likely contributes to this effect, offering more contact area for dye loading and promoting a higher uptake.

Moreover, HFMN patches with a nominal needle height of 500 μm showed an overall reduction of 8.1 ± 8.0% in needle height compared to the initial value after insertion into the agarose gel across all conditions. Specifically, longer insertion times of 45 and 60 s resulted in a slightly higher reduction of 9.7 ± 3.0%, while shorter times of 15 and 30 s led to a reduction of 6 ± 2.7%. Figure 2c−f shows the average loaded needle heights at different conditions. As insertion depth and holding time increased, the average loaded height also increased. As the insertion depth rises from 100 to 400 μm and holding times are extended, the average loaded height reached between 260 and 280 μm. For example, at 15 s (Figure 2c), the loaded height ranged from 114 ± 51 μm to 264 ± 44 μm, while at 60 s (Figure 2f), it ranged from 226 ± 50 to 281 ± 66 μm. These results demonstrate the significant impact of both insertion depth and holding time on HFMN loading.

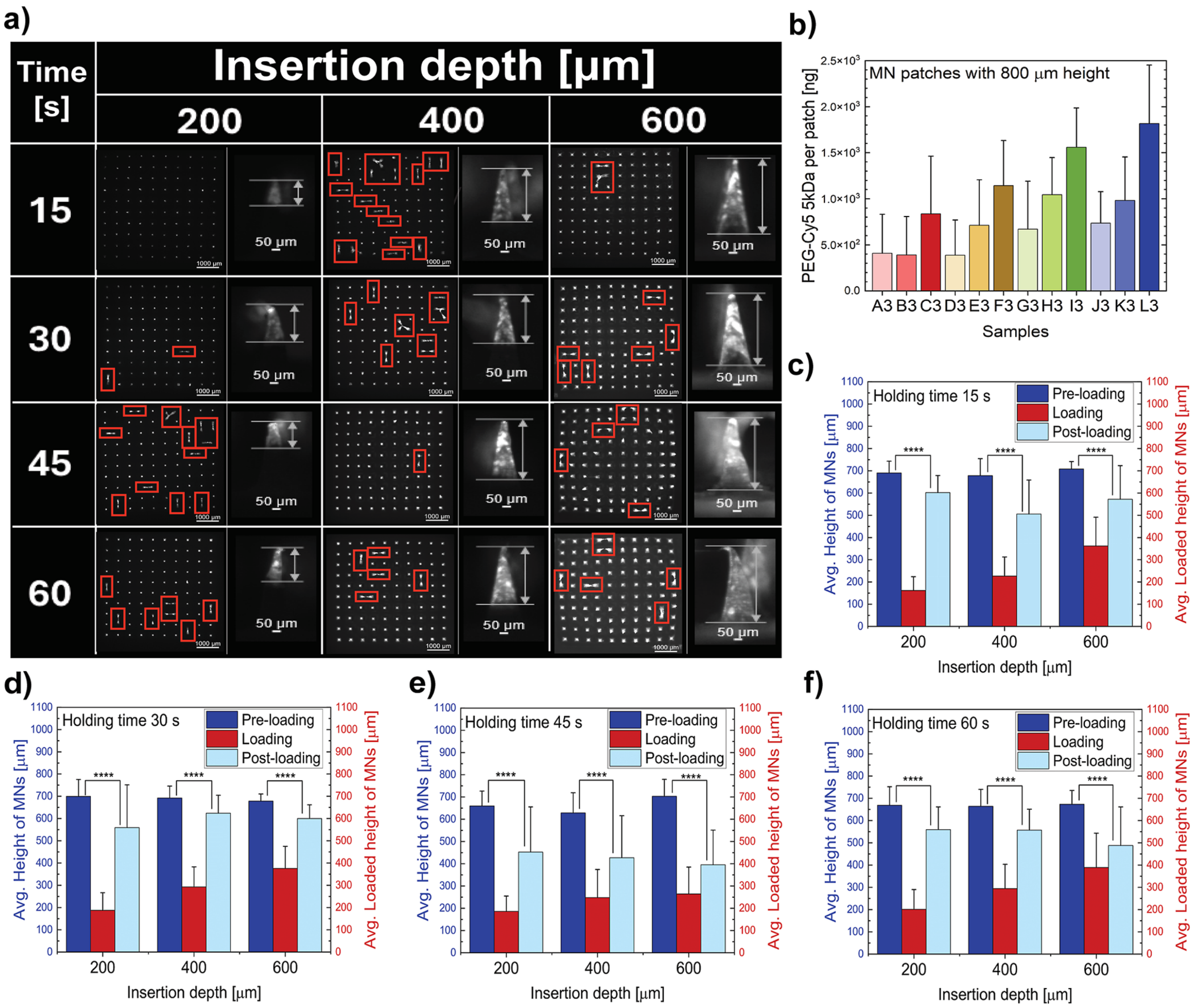

Figure 3. (a) Images of HFMN patches with a needle height of 800 *μ*m inserted into 1% w/v agarose gels containing 40 *μ*M PEG-Cy5 (5 kDa) at varying depths from 200, 400, and 600 *μ*m and held at each depth for 15, 30, 45, and 60 s. Images captured at zero-degree angle, with insets showing 90-degree zoomed views to highlight loaded needle tips under respective conditions. Structural defects, such as needle twisting or fusion, are indicated within the red boxes. (b) Quantification of PEG-Cy5 (5 kDa) dye loaded in MN patches under different insertion depths and hold times. The conditions included 200 *μ*m insertion depth for 15 s (A3), 30 s (B3), 45 s (C3), and 60 s (D3); 100 *μ*m insertion depth for 15 s (E3), 30 s (F3), 45 s (G3), and 60 s (H3); and 200 *μ*m insertion depth for 15 s (I3), 30 s (J3), 45 s (K3), and 60 s (L3). Comparison of MN patch height before loading (dark blue) and after loading (light blue), with the average loaded height (red) achieved at varying insertion depths and holding times: 15 s (c), 30 s (d), 45 s (e), and 60 s (f). Error bars, mean ± SD (*n* = 3).

To further optimize the post-manufacturing approach, we tested MN patches with an 800 *μ*m needle height inserted into agarose gels at depths of 200, 400, and 600 *μ*m, with holding times of 15, 30, 45, and 60 s. Figure 3a shows an increased needle array brightness with deeper depths and longer holding times, accompanied by higher needle torsion or fusion defects. Quantitative analysis (Figure 3b) confirms that the PEG-Cy5 uptake increased with longer holding times. Figure 3c−f shows that as the insertion depth increased from 200 to 600 *μ*m, the average loaded height also rose, reaching 342 ± 73 at 600 *μ*m after 30 s. However, at 45 and 60 s, the average loaded height at 600 *μ*m decreased to 220 ± 97 *μ*m and 325 ± 130 *μ*m, respectively. This trend may result from a 23.3 ± 11.2% reduction in needle height across all conditions, with more pronounced reductions (30.1 ± 11.3%) at 45 and 60 s. In contrast, the reduction is less pronounced (16.5 ± 6%.) at 15 and 30 s. Despite the reduction in needle height, dye uptake remained higher with deeper insertion and longer holding times. The reduction in needle height, potentially caused by needle torsion or fusion, may affect drug release efficiency in the skin when using these patches.

Comparative analysis of the HFMN patch with needle heights of 250 *μ*m, 500 *μ*m, and 800 *μ*m reveals distinct performance characteristics. The 250 *μ*m patches showed consistent dye uptake, peaking at 1052 ± 633 ng after 60 s at a 200 *μ*m insertion depth. Prolonged holding at deeper depths improved the dye absorption. However, structural defects, such as needle twisting and the fusion of multiple needles, were observed at greater insertion depths and holding times. These defects could interfere with the drug release efficiency and

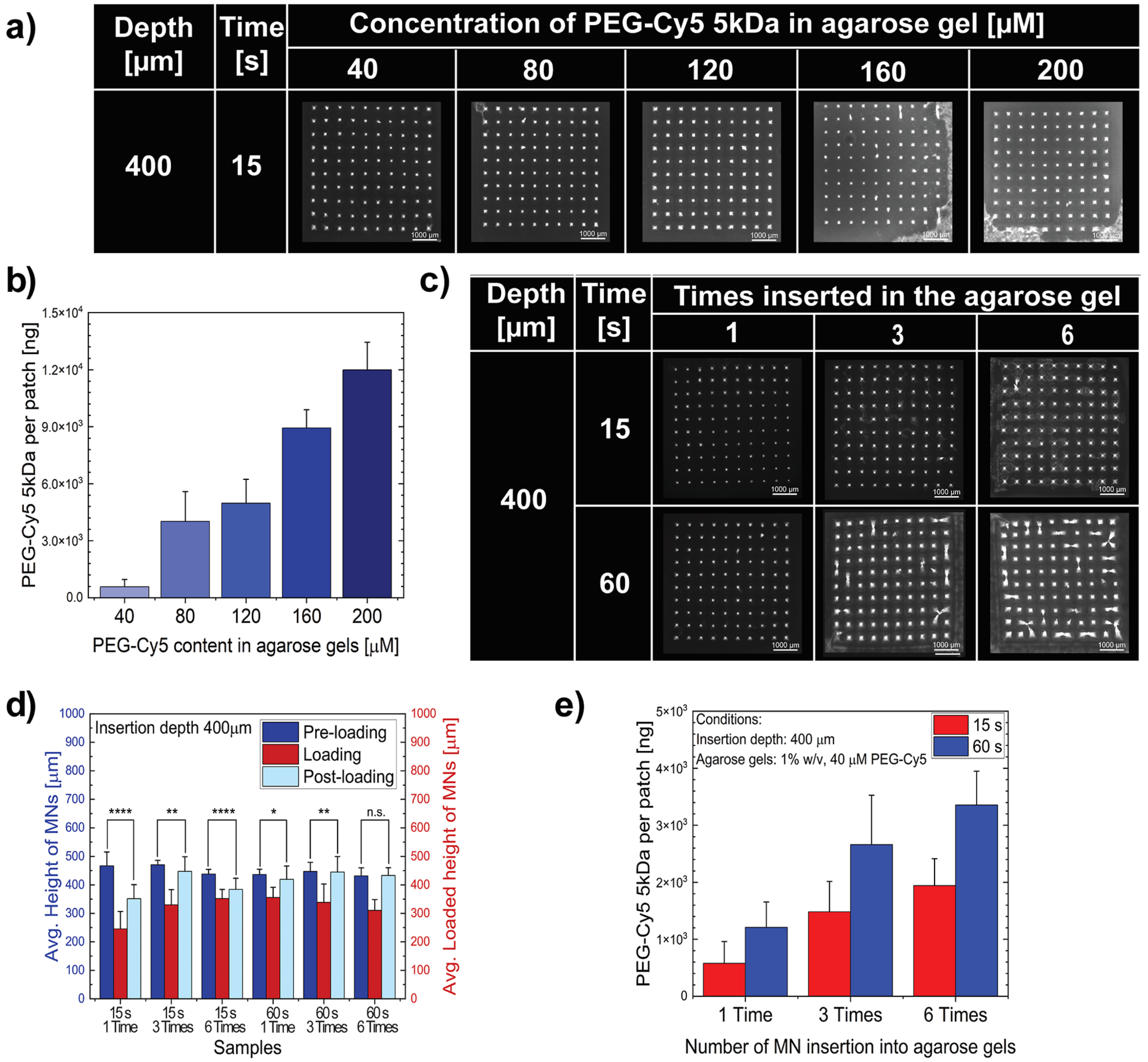

Figure 4. (a) Images at zero-degree angles of HFMN patches inserted into agarose gels containing PEG-Cy5 (5 kDa) at concentrations of 40, 80, 120, 160, and 200 μM. The needles were inserted to a depth of 400 μm and held for 15 s. Structural defects, such as needle twisting or fusion, as well as dye absorption in the patch's base substrate, are indicated within the red boxes. (b) Quantification of PEG-Cy5 loaded into HFMN patches under the same conditions as (a). (c) Comparative images of HFMNs inserted into agarose gels containing 40 μM PEG-Cy5. The patches were inserted to a depth of 400 μm and held for 15 and 60 s. The structural integrity of the needles was assessed after one, three, and six insertions. Structural defects, such as needle twisting or fusion, as well as dye absorption in the patch's base substrate, are indicated within the red boxes. (d) Comparison of HFMN patch height before loading (dark blue) and after loading (light blue), alongside the average loaded height (red). The measurements correspond to the same conditions as (c) at a 400 μm insertion depth, with holding times of 15 and 60 s. (e) Quantification of PEG-Cy5 (5 kDa) dye loaded into HFMN patches under the conditions described in (c). The analysis compares 15 s and 60 s holding times after one, three, and six insertions into the agarose gels. Error bars, mean ± SD (n = 3 HFMN patches for each condition).

hinder skin penetration. Despite a manageable 19.8 ± 11.9% reduction in needle height after loading, the 250 μm patches' limited insertion depth and smaller loaded needle height (maximum 174 ± 44 μm) reduced their effectiveness in deeper agarose gel penetration.

On the other hand, the 500 μm needle patches offered improved dye absorption, reaching a maximum uptake of 1209 ± 447 ng at 60 s and 400 μm insertion depth. Longer holding times and deeper insertion depths enhanced the dye uptake without significant structural defects. These patches exhibited an 8.1 ± 8.0% reduction in needle height post-loading and higher loaded needle heights (up to 281 ± 66 μm) with greater fluorescence intensity compared to the 250 μm design. Their balanced performance and minimal deformation make them ideal options for further applications demanding medium penetration depth and efficient drug delivery.

Finally, the 800 μm needle patches showed the highest dye uptake of 1816 ± 637 ng at 60 s and 600 μm insertion depth but showed significant structural issues, including a 23.3 ± 11.2% height reduction and increased torsion and fusion

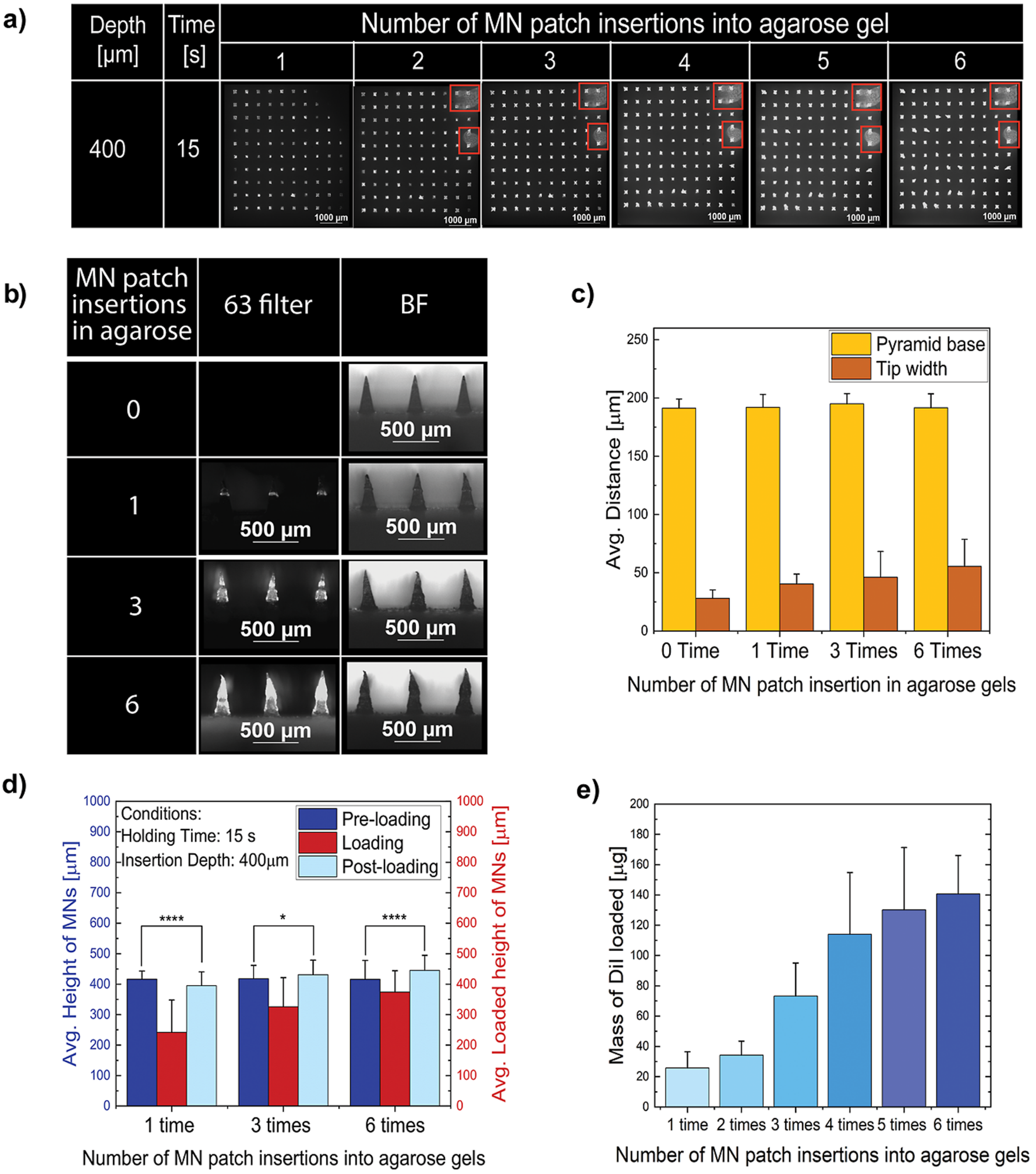

Figure 5. (a) Comparison of zero-degree images of HFMN patches inserted at a 400 *µ*m depth for a 15 s holding time across multiple insertions: one, two, three, four, five, and six times. Structural defects, such as needle twisting or fusion, as well as dye absorption in the patch's base substrate, are indicated within the red boxes. (b) Zoomed-in images of HFMN patches captured at a 90-degree angle after multiple insertions into agarose gels at a 400 *µ*m depth with a 15 s holding time. Fluorescence images acquired using the 63-filter set reveal LNP distribution within the needles, while corresponding bright-field (BF) images display structural integrity and deformation. (c) Quantification of the distance from the microneedle pyramid base and the tip width after insertion into agarose gels, indicating potential structural deformation caused by repeated applications. (d) Comparison of HFMN patch height before loading (dark blue) and after loading (light blue), with the average loaded height (red). Measurements correspond to a 400 *µ*m insertion depth and 15 s holding times after one, three, and six insertions. (e) Quantification of MC3-DOPE-DiI LNPs loaded into HFMN patches under the same conditions as (a). Data are presented for one, two, three, four, five, and six insertions into the agarose gels. Error bars, mean ± SD (*n* = 3 HFMN patches for each condition).

defects. Despite their high loading capacity (up to 325 ± 130 μm), their mechanical instability limits reliability for precise applications. In contrast, the 500 μm patches with balanced performance and minimal deformation were selected as the most suitable candidate for further experiments.

The following experiments focused on optimizing the drug uptake in 500 μm HFMN patches by increasing the PEG-Cy5 concentration and testing multiple insertions. PEG-Cy5 was gradually increased to 200 μM in a 1% w/v agarose gel, with patches inserted to 400 μm for 15 s, as detailed in Table 2. This depth and duration were chosen to minimize the structural defects. Microscopic images in Figure 4a show increased needle brightness with higher PEG-Cy5 concentrations. However, when the patches were inserted into gels with concentrations of 80 μM and above, dye uptake was observed at the base substrate of the patches, suggesting potential drug waste.[17]

Figure 4b illustrates the loading capacity of the MNs at various PEG-Cy5 concentrations. At 40 μM, the loading was 578 ± 383 ng, increasing significantly with PEG-Cy5 concentration on the agarose gels to 4019 ± 1577 ng at 80 μM and 4975 ± 1263 ng at 120 μM. At higher concentrations—160 μM and 200 μM—the loading further increased to 8939 ± 954 ng and 11,988 ± 1465 ng, respectively. These elevated values likely reflect not only greater loading within the MNs but also increased dye absorption by the patch's base substrate. This off-target uptake becomes more evident at concentrations of ≥80 μM, as shown in Figure 4a, and may result in an overestimation of the actual payload delivered into the needle region. These findings demonstrate the impact of drug concentration in the agarose gels on loading efficiency while maintaining a fixed insertion depth and holding time. They emphasize the importance of identifying an optimal concentration range that maximizes loading into the MNs while minimizing waste due to nonspecific absorption by the patch base. Notably, 578 ng may represent the maximum loading capacity confined to the MN tips under these conditions, without significant diffusion into the base. Striking this balance is critical for improving the cost-efficiency and reproducibility of MN-mediated delivery, particularly when working with expensive or sensitive therapeutics.

Furthermore, we evaluated multiple insertions of 500 μm HFMN patches into agarose gels containing PEG-Cy5 at a concentration of 40 μM to enhance the loading capacity. Patches were inserted up to six times at 400 μm depth, with 15 s and 60 s holding times, as shown in Table 3. This approach assessed total loading capacity and structural integrity after repeated insertions. Figure 4c presents zero-degree images of patches after one, three, and six insertions into agarose gels. After three insertions with 60 s hold, needle twisting and fusion appeared, while six insertions with 15 s hold caused only minor defects. In both cases, staining in the substrate base indicated PEG-Cy5 absorption, with more pronounced absorption at 60 s than at 15 s. Figure 4d shows the needle height before and after each insertion. With a 15 s holding time, the needle height decreased by 18% from its initial height after six insertions. Despite this reduction, the loaded needle height remained stable, rising from 245 ± 61 μm to 352 ± 32 μm. In contrast, with a 60 s holding time, the loaded height declined from 355 ± 36 μm to 310 ± 38 μm after six insertions due to increased needle fusion, compromising the overall structural integrity of the patch. Figure 4e quantifies PEG-Cy5 uptake, showing a steady increase with a 15 s holding time. The dye uptake was 578 ± 382 ng after one insertion, 1483 ± 533 ng after three insertions, and 1945 ± 470 ng after six insertions. For a 60 s holding time, the dye uptake rose from 1209 ± 447 ng to 3356 ± 591 ng after six insertions but caused structural defects including needle fusion and twisting, as well as increased dye absorption in the patch's base substrate. Due to these limitations, the 15 s holding time with multiple insertions (ranging from one to six) was selected for further studies with LNPs.

After optimization of the loading approach, 500 μm HFMNs were tested with LNPs containing DiI as a fluorescent tracer. As detailed in Table 4, patches were inserted to a depth of 400 μm for 15 s, with a 5 min interval between up to six insertions to allow drying. This method ensured efficient loading while maintaining the structural integrity. Figure 5a shows zero images of patches after one−six insertions, with a progressive increase in fluorescence, indicating enhanced LNP loading. Fluorescence on the base substrate suggests off-target loading. Minor structural defects, such as slight needle twisting, were observed with increasing numbers of insertions, as shown in Figure 5b. This observation is supported by the analysis of the MN pyramid base distance (Figure 5c), which remained stable at approximately 190 μm—even after six insertions into agarose gels—and was comparable to that of prefabricated patches. A modest increase in tip width was also detected, rising from 28 ± 7 μm in prefabricated patches to 40 ± 9 μm after one insertion. With additional insertions, the tip width remained stable, measuring 46 ± 22 μm after three applications and 55 ± 23 μm after six. This slight broadening did not appear to compromise the structural integrity of the MNs. Overall, the findings indicate that the integrity of the HFMN patches is largely preserved after multiple insertions into agarose gels, and the minimal deformation observed is unlikely to negatively affect drug release performance when applied to the skin. Additionally, the needle height before and after loading remained relatively unchanged, maintaining values close to the initial height, as shown in Figure 5d. However, the average loaded height increased from 280 ± 118 μm after one insertion to 359 ± 65 and 374 ± 70 μm after three and six insertions, respectively. These results are consistent with the quantification data of MC3-DOPE-DiI LNPs shown in Figure 5e, where the LNP loading increased from 26 ± 11 μg after one insertion to 141 ± 25 μg after six insertions.

Recent post-manufacturing loading approaches have primarily focused on surface-coating methods applied to solid MNs, including dip-coating, spray-coating, and inkjet printing.[17] While these techniques are relatively simple, they range from basic processes with high drug waste to more elaborate procedures designed to reduce such losses. Although they have been successfully used for the delivery of small molecules and vaccines, they generally allow only modest drug loading, ranging from a few nanograms to hundreds of micrograms, and are often associated with uneven coatings and drug loss during handling or skin insertion. In contrast, the strategy developed in this study leverages the intrinsic swelling and absorptive capacity of HFMNs to facilitate the volumetric-matrix-based loading of nanoparticles. Using this approach, up to 140 μg of mRNA-LNPs was successfully integrated into the HFMN patches after six repeated insertions at 400 μm insertion depth, 15 s per insertion. This represents a substantially higher payload compared to conventional surface-coating methods.

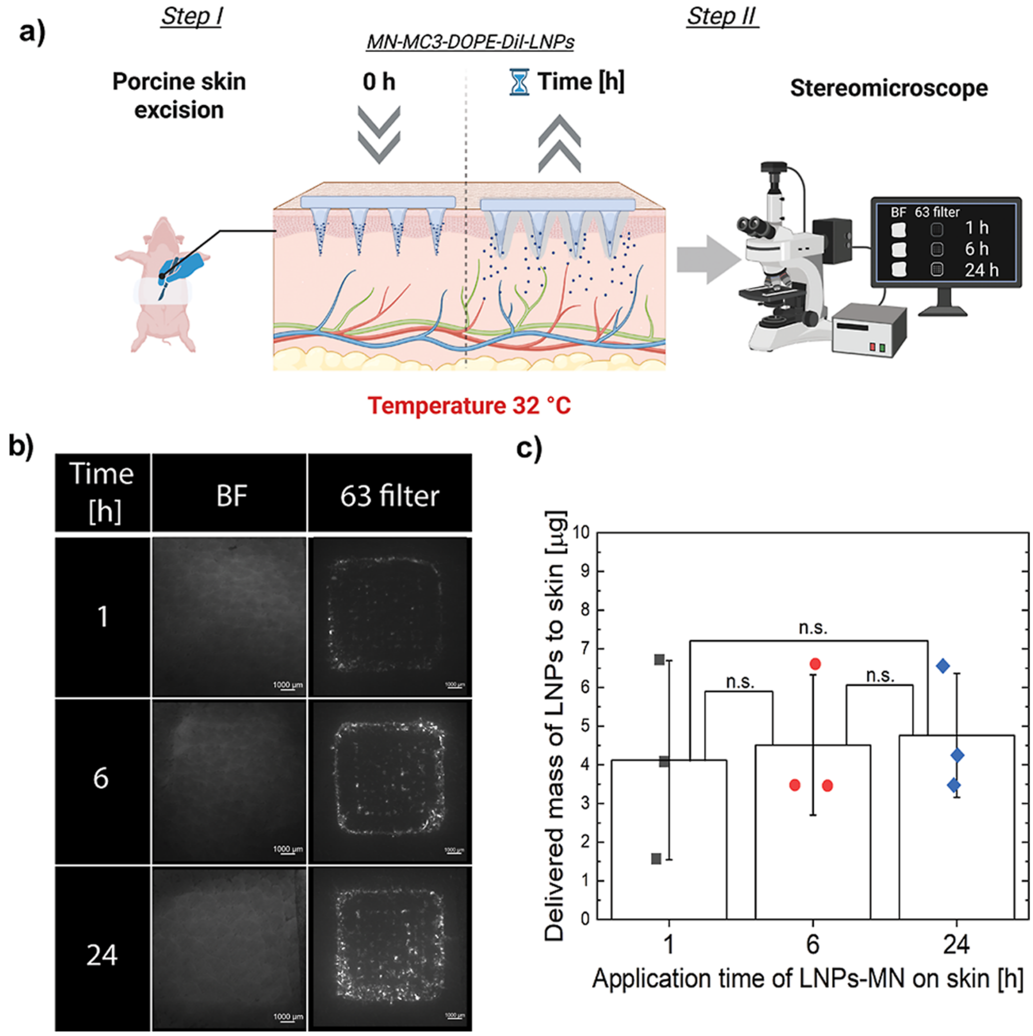

Figure 6. (a) Schematic representation of the drug delivery assessment conducted in an ex vivo experiment using porcine skin samples. (b) Images of porcine skin samples after contact with MC3-DOPE-DiI LNP-loaded HFMNs at different time points: 1, 6, and 24 h, captured under the brightfield (BF) mode and the fluorescence mode using the 63 filter. (c) Quantification of the delivered amount of MC3-DOPE-DiI LNPs into the skin at 1, 6, and 24 h. Data are presented as mean ± SD (*n* = 3 skin samples per time point).

Furthermore, this integration was achieved under mild ambient conditions using compression-assisted insertion, which also enabled spatially defined loading within the MN patches. Such gentle processing is particularly advantageous for preserving the structure and integrity of LNPs. This method thus provides a complementary and potentially superior alternative for applications requiring the delivery of sensitive or complex therapeutics, such as mRNA.

To evaluate the RNA delivery, MC3-DOPE-DiI LNP-loaded HFMNs were applied to porcine skin and incubated at 32 °C, to mimic physiological conditions, for 1, 6, and 24 h. At each time point, patches were carefully removed, and skin samples were visualized using a stereomicroscope, Figure 6a. Fluorescent images, depicted in Figure 6b, demonstrated a time-dependent release of LNPs into the skin, with the fluorescence intensity increasing over time. This indicated effective and progressive delivery into the skin. HFMNs loaded with approximately 140 µg of MC3-DOPE-DiI LNPs released 4 µg upon skin application, suggesting a limited drug release efficiency (~2.9%).

Fluorescence-based stereomicroscopy is a widely used method for qualitative and semiquantitative evaluation of nanoparticle release in ex vivo skin models.[47] Although the study included only three sampling points, they were selected to capture representative early, intermediate, and prolonged release phases under physiologically relevant conditions. This allowed for proof-of-concept validation of the LNP delivery. Future work will include more frequent sampling and quantitative techniques to better characterize the release kinetics.

Despite the evident increase in fluorescence intensity observed in skin samples imaged by using fluorescence-based stereomicroscopy (Figure 6b), the subsequent quantification of LNPs delivered into the tissue resulted in relatively low recovery values (Figure 6c). Several factors may explain this discrepancy. The low recovery of DiI after is likely due to the limitations in the extraction method.

MC3-DOPE-DiI LNPs exhibited a hydrodynamic diameter of 83 ± 7 nm before loading (polydispersity index [PDI] = 0.128), which increased to 648 ± 96 nm (PDI = 0.209) after extraction from HFMN patches. Blank patches (without LNPs) yielded particles of 574 ± 34 nm. These results suggest that the measured particle size postextraction is largely influenced by the method of extraction, which may affect the

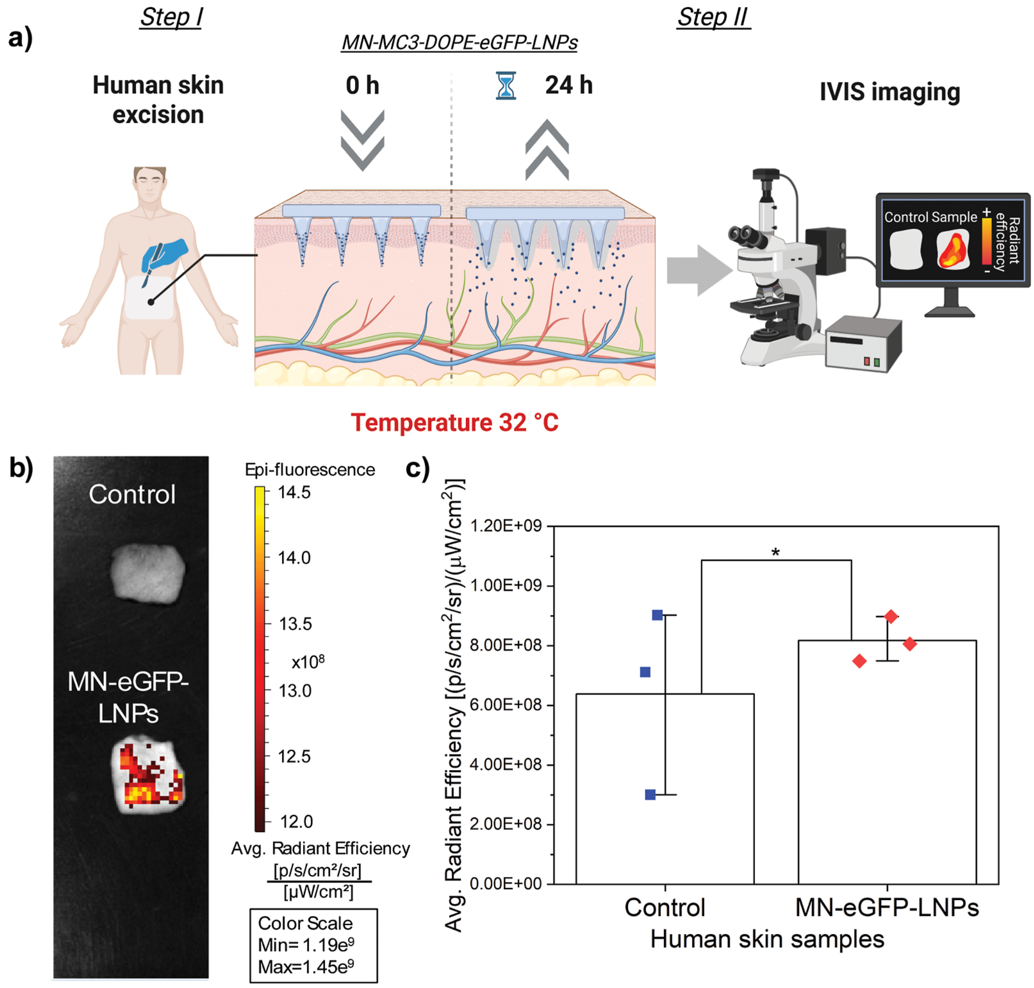

Figure 7. (a) Schematic representation of the IVIS imaging setup for analyzing eGFP transfection in human skin excision samples. (b) IVIS images of human skin samples: control samples treated with blank HFMN patches and treated samples transfected with eGFP using MC3-DOPE-eGFP LNP-loaded HFMN patches. (c) Quantification of average radiant efficiency in human skin samples from three different patients, comparing control and treated groups.

particle size. The zeta potential of the LNPs shifted slightly from −1.4 ± 0.4 mV prior to loading to −8.1 ± 6.2 mV after extraction while the hydrogel matrix alone exhibited a surface charge of −6.58 ± 3.33 mV. All values remained near neutral (−10 to +10 mV), suggesting minimal aggregation[48] (Figure S1).

Functional delivery was confirmed through ex vivo imaging studies. HFMN patches were then loaded with MC3-DOPE-eGFP LNPs using a multi-insertion approach. HFMN patches underwent up to six insertions into agarose gels, each lasting 15 s at a 400 μm, with 10 μL of air-dried MC3-DOPE-eGFP LNPs applied per insertion and a 5 min drying interval. The loaded patches were then applied to freshly excised abdominal skin from three independent human donors (Figure 7a). Imaging analysis revealed that treated samples with MC3-DOPE-eGFP LNP-loaded HFMNs exhibited significantly higher fluorescence intensity, measured as the average radiant efficiency, compared to control samples treated with blank HFMN patches (Figure 7b). However, the difference in quantified average radiant efficiency was less pronounced (Figure 7c), which may be attributed to skin autofluorescence, variability in tissue composition, and dilution of the localized signal during ROI-based quantification. These findings confirm functional mRNA expression in human skin using MC3-DOPE-eGFP LNP-loaded HFMNs, highlighting the potential of this system for localized and efficient genetic material delivery.

■ CONCLUSION

This study presents a novel, spatially controlled method for loading mRNA-encapsulated LNPs into HFMN patches using a texture analyzer in compression mode. By systematically varying parameters such as insertion depth, duration, dye concentration, and repeated insertions. This method enables efficient and reproducible LNP loading, while maintaining the structural integrity of MNs. The hydrogel's absorption capacity ensures precise uptake with minimal material waste, requiring only small volumes per patch. The selected 500 μm HFMN patches proved to be optimal for LNP uptake, further enhanced by repeated insertions. The successful ex vivo delivery of LNPs into human skin and subsequent GFP transfection confirm the utility of this approach for the precise and effective delivery of nucleic acid therapeutics, while the current optimization was conducted through sequential experimentation to isolate and assess how individual variables affect LNP loading, patch integrity, and delivery performance. Future studies will incorporate advanced statistical methods such as response surface methodology within a Design of

Experiments framework. This approach is expected to enhance predictive capabilities, reduce experimental workload, and improve reproducibility under more physiologically relevant conditions, especially as we advance toward in vivo studies for gene editing applications. Altogether, this work highlights the potential of post-manufacturing loading strategies for advanced transdermal applications, providing a minimally invasive platform for the targeted delivery of sensitive therapeutics such as LNPs. The findings pave the way for future clinical and translational efforts to utilize HFMN patches for vaccine delivery, gene therapy, and RNA-based therapeutics.

■ ASSOCIATED CONTENT

Supporting Information

The Supporting Information is available free of charge at https://pubs.acs.org/doi/10.1021/acs.molpharmaceut.5c00403.

> Physicochemical characterization data of the MC3-DOPE-DiI LNPs, specifically the hydrodynamic diameter and zeta potential measurements before and after loading into the HFMN patches (PDF)

■ AUTHOR INFORMATION

Corresponding Author

Davide Brambilla – *Faculty of Pharmacy, University of Montreal, Montreal H3T 1J4, Canada;* orcid.org/0000-0002-5749-1125; Email: davide.brambilla@umontreal.ca

Authors

Alfonso Arguello – *Faculty of Pharmacy, University of Montreal, Montreal H3T 1J4, Canada*

Gaurav Sadhnani – *Berlin Institute of Health @ Charité Universitätsmedizin, Berlin 10117, Germany*

Jerry Leung – *Department of Biochemistry and Molecular Biology, University of British Columbia, Vancouver V6T 1Z3, Canada*

Fatma Moawad – *Faculty of Pharmacy, University of Montreal, Montreal H3T 1J4, Canada;* orcid.org/0000-0002-1451-9730

Pieter R. Cullis – *Department of Biochemistry and Molecular Biology, University of British Columbia, Vancouver V6T 1Z3, Canada;* orcid.org/0000-0001-9586-2508

Sarah Hedtrich – *Berlin Institute of Health @ Charité Universitätsmedizin, Berlin 10117, Germany; Faculty of Pharmaceutical Sciences, University of British Columbia, Vancouver V6T 1Z3, Canada; School of Biomedical Engineering and Centre for Blood Research & Life Science Institute, Life Sciences Centre, University of British Columbia, Vancouver V6T 2B9, Canada;* orcid.org/0000-0001-6770-3657

Complete contact information is available at: https://pubs.acs.org/10.1021/acs.molpharmaceut.5c00403

Notes

The authors declare no competing financial interest.

■ REFERENCES

(1) Akhtar, N.; Singh, V.; Yusuf, M.; Khan, R. A. Non-invasive drug delivery technology: Development and current status of transdermal drug delivery devices, techniques and biomedical applications. *Biomed. Tech.* **2020**, *65*, 243–272.

(2) Al-Qallaf, B.; Das, D. B. Optimizing microneedle arrays for transdermal drug delivery: Extension to non-square distribution of microneedles. *J. Drug Target* **2009**, *17* (2), 108–122.

(3) Vaseem, R. S.; D'cruz, A.; Shetty, S.; Hafsa; Vardhan, A.; Shenoy R, S.; Marques, S. M.; Kumar, L.; Verma, R. Transdermal Drug Delivery Systems: A Focused Review of the Physical Methods of Permeation Enhancement. *Adv. Pharm. Bull.* **2023**, *14*, 67.

(4) Ita, K. Transdermal delivery of drugs with microneedles—potential and challenges. *Pharmaceutics* **2015**, *7* (3), 90–105.

(5) Maia, M.; Jesus, S.; Borges, O. Optimizing insulin therapy: Are microneedles a viable alternative to subcutaneous insulin injection? *J. Drug Deliv Sci. Technol.* **2024**, *101*, 106229.

(6) Alkilani, A. Z.; Nasereddin, J.; Hamed, R.; Nimrawi, S.; Hussein, G.; Abo-Zour, H.; Donnelly, R. F. Beneath the Skin: A Review of Current Trends and Future Prospects of Transdermal Drug Delivery Systems. *Pharmaceutics* **2022**, *14*, 1152.

(7) Larrañeta, E.; Lutton, R. E. M.; Woolfson, A. D.; Donnelly, R. F. Microneedle arrays as transdermal and intradermal drug delivery systems: Materials science, manufacture and commercial development. *Mater. Sci. Eng., R* **2016**, *104*, 1.

(8) Hao, Y.; Li, W.; Zhou, X. L.; Yang, F.; Qian, Z. Y. Microneedles-based transdermal drug delivery systems: A review. *J. Biomed. Nanotechnol.* **2017**, *13* (12), 1581–1597.

(9) Gowda, B. H. J.; Ahmed, M. G.; Sahebkar, A.; Riadi, Y.; Shukla, R.; Kesharwani, P. Stimuli-Responsive Microneedles as a Transdermal Drug Delivery System: A Demand-Supply Strategy. *Biomacromolecules* **2022**, *23*, 1519–1544.

(10) Yan, L.; Alba, M.; Tabassum, N.; Voelcker, N. H. Micro- and Nanosystems for Advanced Transdermal Delivery. *Adv. Ther (Weinh)* **2019**, *2*, 1900141.

(11) Rabiei, M.; Kashanian, S.; Samavati, S. S.; Jamasb, S.; McInnes, S. J. P. Nanomaterial and advanced technologies in transdermal drug delivery. *J. Drug Target* **2020**, *28* (4), 356–367.

(12) Wang, X.; Cheng, W.; Su, J. Research Progress of Extracellular Vesicles-Loaded Microneedle Technology. *Pharmaceutics* **2024**, *16*, 326.

(13) Lin, S.; Cao, Y.; Chen, J.; Tian, Z.; Zhu, Y. Recent advances in microneedles for tumor therapy and diagnosis. *Appl. Mater. Today* **2021**, *23*, 101036.

(14) Wu, C.; Yu, Q.; Huang, C.; Li, F.; Zhang, L.; Zhu, D. Microneedles as Transdermal Drug Delivery System for Enhancing Skin Disease Treatment. *Acta Pharm. Sin. B* **2024**, *14*, 5161–5180.

(15) Gupta, J.; Gill, H. S.; Andrews, S. N.; Prausnitz, M. R. Kinetics of skin resealing after insertion of microneedles in human subjects. *J. Controlled Release* **2011**, *154* (2), 148–155.

(16) Haj-Ahmad, R.; Khan, H.; Arshad, M.; Rasekh, M.; Hussain, A.; Walsh, S.; Li, X.; Chang, M. W.; Ahmad, Z. Microneedle coating techniques for transdermal drug delivery. *Pharmaceutics* **2015**, *7*, 486–502.

(17) Ingrole, R. S. J.; Gill, H. S. Microneedle coating methods: A review with a perspective. *J. Pharmacol. Exp. Ther.* **2019**, *370* (3), 555–569.

(18) Parhi, R. Recent advances in 3D printed microneedles and their skin delivery application in the treatment of various diseases. *J. Drug Delivery Sci. Technol.* **2023**, *84*, 104395.

(19) Long, L.; Ji, D.; Hu, C.; Yang, L.; Tang, S.; Wang, Y. Microneedles for in situ tissue regeneration. *Mater Today Bio* **2023**, *19*, 100579.

(20) Moawad, F.; Pouliot, R.; Brambilla, D. Dissolving microneedles in transdermal drug delivery: A critical analysis of limitations and translation challenges. *J Control Release* **2025**, *383*, 113794.

(21) Makvandi, P.; Kirkby, M.; Hutton, A. R. J.; Shabani, M.; Yiu, C. K. Y.; Baghbantaraghdari, Z.; Jamaledin, R.; Carlotti, M.; Mazzolai, B.; Mattoli, V.; et al. Engineering Microneedle Patches for Improved Penetration: Analysis, Skin Models and Factors Affecting Needle Insertion. *Nanomicro Lett.* **2021**, *13* (1), 93.

(22) Lee, K. J.; Jeong, S. S.; Roh, D. H.; Kim, D. Y.; Choi, H. K.; Lee, E. H. A practical guide to the development of microneedle

systems—In clinical trials or on the market. *Int. J. Pharm.* **2020**, *573*, 118778.

(23) Sheng, T.; et al. Microneedle-Mediated Vaccination: Innovation and Translation. *Adv. Drug Deliv Rev.* **2021**, *179*, 113919.

(24) Li, Y.; Bi, D.; Hu, Z.; Yang, Y.; Liu, Y.; Leung, W. K. Hydrogel-Forming Microneedles with Applications in Oral Diseases Management. *Matrerials* **2023**, *16*, 4805.

(25) Le, Z.; et al. Design principles of microneedles for drug delivery and sampling applications. *Mater. Today* **2023**, *63*, 137−169.

(26) Turner, J. G.; White, L. R.; Estrela, P.; Leese, H. S. Hydrogel-Forming Microneedles: Current Advancements and Future Trends. *Macromol. Biosci.* **2021**, *21*, 2000307.

(27) Fan, L.; Zhang, X.; Nie, M.; Xu, Y.; Wang, Y.; Shang, L.; Zhao, Y.; Zhao, Y. Photothermal Responsive Microspheres-Triggered Separable Microneedles for Versatile Drug Delivery. *Adv. Funct. Mater.* **2022**, *32*, 2110746.

(28) Hardy, J. G.; et al. Hydrogel-Forming Microneedle Arrays Made from Light-Responsive Materials for On-Demand Transdermal Drug Delivery. *Mol. Pharmaceutics* **2016**, *13* (3), 907−914.

(29) Jia, T.; et al. Silk fibroin/chitosan pH-sensitive controlled microneedles. *J. Mater. Sci.* **2023**, *58* (46), 17711−17725.

(30) Donnelly, R. F.; et al. Hydrogel-forming microneedle arrays for enhanced transdermal drug delivery. *Adv. Funct. Mater.* **2012**, *22* (23), 4879−4890.

(31) Wang, Y.; et al. An injectable extracellular matrix-mimicking conductive hydrogel for sequential treatment of ischemic stroke. *Chem. Eng. J.* **2024**, *502*, 158039.

(32) Bolsoni, J.; et al. Lipid Nanoparticle-Mediated Hit-and-Run Approaches Yield Efficient and Safe In Situ Gene Editing in Human Skin. *ACS Nano* **2023**, *17* (21), 22046−22059.

(33) Xu, L.; Wang, X.; Liu, Y.; Yang, G.; Falconer, R. J.; Zhao, C. X. Lipid Nanoparticles for Drug Delivery. *Adv. Nanobiomed Res.* **2022**, *2*, 2100109.

(34) Thi, T. T. H.; Suys, E. J. A.; Lee, J. S.; Nguyen, D. H.; Park, K. D.; Truong, N. P. Lipid-based nanoparticles in the clinic and clinical trials: From cancer nanomedicine to COVID-19 vaccines. *Vaccines (Basel)* **2021**, *9* (4), 359.

(35) Reichmuth, A. M.; Oberli, M. A.; Jaklenec, A.; Langer, R.; Blankschtein, D. mRNA vaccine delivery using lipid nanoparticles. *Ther Deliv* **2016**, *7* (5), 319−334.

(36) Liu, Y.; Huang, Y.; He, G.; Guo, C.; Dong, J.; Wu, L. Development of mRNA Lipid Nanoparticles: Targeting and Therapeutic Aspects. *Int. J. Mol. Sci.* **2024**, *25* (18), 10166.

(37) Noh, I.; Lee, K.; Rhee, Y. S. Microneedle systems for delivering nucleic acid drugs. *J. Pharm. Investig.* **2022**, *52*, 273−292.

(38) Crommelin, D. J. A.; Anchordoquy, T. J.; Volkin, D. B.; Jiskoot, W.; Mastrobattista, E. Addressing the Cold Reality of mRNA Vaccine Stability. *J. Pharm. Sci.* **2021**, *110* (3), 997−1001.

(39) Cheng, F.; et al. Research Advances on the Stability of mRNA Vaccines. *Viruses* **2023**, *15* (3), 668.

(40) Kolhe, P.; Amend, E.; Singh, S. K. Impact of freezing on pH of buffered solutions and consequences for monoclonal antibody aggregation. *Biotechnol. Prog.* **2010**, *26* (3), 727−733.

(41) Packer, M.; Gyawali, D.; Yerabolu, R.; Schariter, J.; White, P. A novel mechanism for the loss of mRNA activity in lipid nanoparticle delivery systems. *Nat. Commun.* **2021**, *12* (1), 6777.

(42) Fabre, A. L.; Colotte, M.; Luis, A.; Tuffet, S.; Bonnet, J. An efficient method for long-term room temperature storage of RNA. *European Journal of Human Genetics* **2014**, *22* (3), 379−385.

(43) vander Straeten, A.; et al. A microneedle vaccine printer for thermostable COVID-19 mRNA vaccines. *Nat. Biotechnol.* **2024**, *42* (3), 510−517.

(44) Babity, S.; Couture, F.; Campos, E. V. R.; Hedtrich, S.; Hagen, R.; Fehr, D.; Bonmarin, M.; Brambilla, D. A Naked Eye-Invisible Ratiometric Fluorescent Microneedle Tattoo for Real-Time Monitoring of Inflammatory Skin Conditions. *Adv. Healthc Mater.* **2022**, *11*, 2102070.

(45) Laszlo, E.; De Crescenzo, G.; Nieto-Argüello, A.; Banquy, X.; Brambilla, D. Superswelling Microneedle Arrays for Dermal Interstitial Fluid (Prote)Omics. *Adv. Funct. Mater.* **2021**, *31* (46), 2106061.

(46) Kulkarni, J. A.; et al. Fusion-dependent formation of lipid nanoparticles containing macromolecular payloads. *Nanoscale* **2019**, *11* (18), 9023−9031.

(47) Limcharoen, B.; Wanichwecharungruang, S.; Banlunara, W.; Darvin, M. E. Seeing through the skin: Optical methods for visualizing transdermal drug delivery with microneedles. *Adv. Drug Deliv. Rev.* **2025**, *217*, 115478.

(48) Mendonça, M. C. P.; Kont, A.; Kowalski, P. S.; O'Driscoll, C. M. Design of lipid-based nanoparticles for delivery of therapeutic nucleic acids. *Drug Discov Today* **2023**, *28* (3), 103505.